

# Self-assembly of metal–organic frameworks and graphene oxide as precursors for lithium-ion battery applications

Xia Yang · Linlin Liu · Ruo Yuan · Chun-Sing Lee

Received: 12 April 2016 / Accepted: 6 September 2016 / Published online: 20 October 2016  
© Springer Science+Business Media Dordrecht 2016

**Abstract** We fabricated composites of Fe<sub>2</sub>O<sub>3</sub>/reduced graphene oxide as lithium-ion batteries anode material with controlled structures by employing self-assembly of metal–organic frameworks (MOFs) and polymer-functionalized graphene oxide as precursors. By electrostatic interaction, the negatively charged MOFs, Prussian Blue (PB), are assembled on poly(-diallyldimethylammonium chloride) (PDDA)-functionalized graphene oxide (positive charge). Then the PB cubes become FeOOH nanosheets when treated with sodium hydroxide. Upon further annealing, the FeOOH nanosheets transform to Fe<sub>2</sub>O<sub>3</sub> nanoparticles while the graphene oxide become reduced graphene oxide simultaneously. It was found that the composites have good performance as anode of lithium-ion

battery. This work shows a new way for self-assembling MOFs and 2D materials.

**Keywords** Metal–organic frameworks (MOFs) · Prussian blue (PB) · Self-assembly · Reduced graphene oxide (rGO) · Lithium-ion battery (LIB) · Energy storage

## Introduction

Metal–organic frameworks (MOFs) are one kind of porous structures which have attracted intense interest due to their various merits such as well-defined frameworks, high surface area, high porosity and tunable pore size. (Li et al. 2009; Furukawa et al. 2010; Zhuang et al. 2012). To widen the applications of MOFs, researchers have prepared composites via MOFs (Jin et al. 2016; Wang et al. 2016; Zhao et al. 2016) or obtained various composites of MOFs with other nanomaterials, such as Pt nanoparticles (Wang et al. 2013a), silica (Tanaka et al. 2012), carbon nanotubes (Yang et al. 2009). By combining unique advantages of graphene oxides (GO) or reduced graphene oxide (rGO) and MOFs, their composites have been applied for adsorptions (Petit and Bandoz 2011), CO<sub>2</sub> uptake (Kumar et al. 2013), precursors for lithium- or sodium-ion batteries (Cao et al. 2014; Liu et al. 2015; Zhang et al. 2013a). In these works, fabrications of the composites often involve

---

**Electronic supplementary material** The online version of this article (doi:10.1007/s11051-016-3589-5) contains supplementary material, which is available to authorized users.

---

X. Yang · R. Yuan  
Key Laboratory of Luminescent and Real-Time Analytical Chemistry, Ministry of Education, College of Chemistry and Chemical Engineering, Southwest University, Chongqing, People's Republic of China  
e-mail: yuanruo@swu.edu.cn

X. Yang · L. Liu · C.-S. Lee (✉)  
Department of Physics and Materials Science, Center of Super-Diamond and Advanced Films (COSDAF), City University of Hong Kong, Kowloon, Hong Kong  
e-mail: apcslee@cityu.edu.hk

synthesizing MOFs in GO or graphene dispersion (Huang et al. 2012; Jahan et al. 2013; Zhou et al. 2014), or physically mixing MOFs and rGO (Bao et al. 2014) etc.

On the other hand, self-assembly method is a powerful alternative for constructing complex material systems. The driving force for the self-assembly is mainly due to electrostatic attraction and complex formation between charged species (Caruso et al. 1998; Boal et al. 2000). In this work, we use a simple self-assembly method to prepare composites with rGO and porous nanoparticles of  $\text{Fe}_2\text{O}_3$ . Firstly, surface of GO was functionalized with poly(diallyldimethylammonium chloride) (PDDA). PDDA is a conducting polymer with strong ionic characteristics which give the modified GO (hereafter refer as p-GO) a positive surface charge. Negatively charged and nanometre-sized cubes of PB crystals (DeLongchamp and Hammond 2004) were then self-assembled on the surface of the p-GO via electrostatic interaction. The PB MOFs were then chemically converted to FeOOH by treating the composite with NaOH. Upon further annealing, the FeOOH becomes porous nanoparticles of  $\text{Fe}_2\text{O}_3$ , while the GO sheets were reduced to rGO sheets (Xia et al. 2012). The composites of porous iron oxides nanoparticles wrapped with rGO were then applied as anodes for lithium-ion batteries and exhibited good performance with specific capacity of  $750 \text{ mAhg}^{-1}$  after 300 cycles at the current density of  $1000 \text{ mA g}^{-1}$ . This work demonstrates a simple method for assembling MOFs with graphene oxide, which should have applications in various fields, such as gas adsorptions, energy storage.

## Experimental

### Materials and reagents

Poly(diallyldimethylammonium chloride) (20 wt%), polyvinylpyrrolidone (PVP, K30, MW  $\sim 40,000$ ) were purchased from Sigma-Aldrich (Hong Kong); graphite,  $\text{K}_4\text{Fe}(\text{CN})_6 \cdot 3\text{H}_2\text{O}$ ,  $\text{NaNO}_3$  and  $\text{KMnO}_4$  were obtained from Advanced Technology and Industrial Co. Ltd. (Hong Kong); HCl,  $\text{H}_2\text{O}_2$  and  $\text{H}_2\text{SO}_4$  were from RCI Labscan limited (Hong Kong).

### Synthesis of $\text{Fe}_2\text{O}_3$ nanoparticles on PDDA-functionalized rGO

GO was prepared using the modified Hummer method (Hummers and Offeman 1958). Two samples of GO (0.1 and 0.2 g, respectively) were added into PDDA solutions (0.5 wt%, 200 mL) and stirred overnight, yielding yellow–brown dispersions. PB cubes were prepared according to the reported method (Zhang et al. 2013b). 0.1 g of PB was put into each of the two dispersions under magnetic stirring for 12 h. The products prepared with PB/GO mass ratios of 1:1 and 1:2 are referred as PB/p-GO1 and PB/p-GO2, respectively. A solution of NaOH (0.5 M, 200 mL) was added into each of the dispersion, and the products are, respectively, abbreviated as FeOOH/p-GO1 and FeOOH/p-GO2. After 1 h, the products were collected by centrifugation and washed with distilled water and ethanol. Then the precursors were dried at  $80^\circ\text{C}$  under vacuum and annealed at  $500^\circ\text{C}$  in  $\text{Ar}/\text{H}_2$  atmosphere for 2 h. The final samples from FeOOH/p-GO1 and FeOOH/p-GO2 are referred as FG1 and FG2. The preparation processes are summarized schematically as Fig. 1.

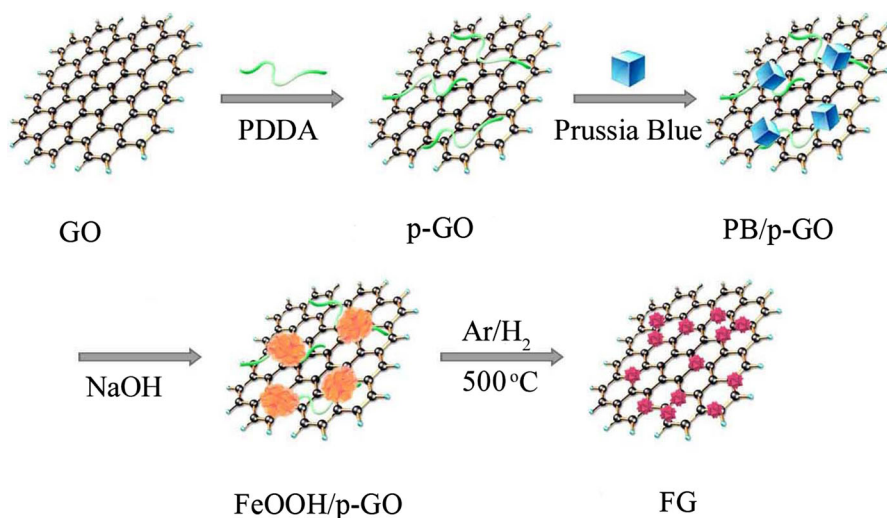
### Synthesis of $\text{Fe}_2\text{O}_3$ nanoparticles

For comparison,  $\text{Fe}_2\text{O}_3$  nanoparticles without graphene oxide wrapping were also prepared. 0.1 g of the PB was added into a sodium hydroxide solution (0.5 M, 200 mL) under stirring. After 1 h, the solution turned brick red. The product was then centrifuged and washed several times with distilled water and absolute ethanol. The product was then dried at  $80^\circ\text{C}$  and annealed at  $500^\circ\text{C}$  in air for 2 h (the product is abbreviated as F).

### Materials characterization

Microstructures of the samples were characterized by scanning electron microscopy (SEM) and transmission electron microscopy (TEM) with, respectively, a Philips XL 30 FEG SEM and a Philips CM200 FEG TEM (operated at 200 kV). Crystal structures of samples were measured with a Philips X'Pert diffractometer using Cu K-alpha radiation. The structure and content of carbon were studied by Fourier transform infrared spectroscopy (BRUKER TENSOR27), Renishaw Raman microscopy (Invia Reflex) and Thermal

**Fig. 1** Schematic diagram showing preparation of Fe<sub>2</sub>O<sub>3</sub>/rGO composite



gravimetric analyser (TGA, METTLER TGA/DSC 1 SF/1382).

#### Electrochemical measurement

To measure the electrochemical properties of the materials, we assembled electrochemical test cells. Firstly, 60 wt% of the product samples, 30 wt% carbon black and 10 wt% carboxymethylcellulose (CMC) were dispersed in distilled water to form a homogeneous slurry. The slurry was then coated on a copper foil to form a film with thickness of 0.1 mm and dried in a vacuum at 90 °C for 12 h. Electrochemical test cells were assembled in a dry argon-filled glove box with less than 1.0 ppm water and oxygen with the coated copper foil as anode. LiPF<sub>6</sub> (1 M) dissolved in an ethylene carbonate (EC) and dimethyl carbonate (DMC) mixture (EC + DMC, 1:1, v/v) was used as the electrolyte. Metal lithium was used as the counter electrode, and one layer of Celgard 2025 (Celgard, Inc., USA) was employed as the separator. The coin-type cells were then discharged and charged at room temperature with a Macc Instruments. Cyclic voltammetry (CV) and electrochemical impedance spectroscopy (EIS) were, respectively, carried out with a CHI 600D and IM6 ZAHNER electrochemical workstations.

#### Results and discussions

As shown in Fig. S1, Fourier transform infrared spectroscopy (FTIR) was used to study the chemistry

structure of PDDA-modified GO (p-GO). Figure. S1a illustrates the FTIR spectra of GO and the oxy-groups of GO including -OH (3413 cm<sup>-1</sup>), C = O (1725 cm<sup>-1</sup>), C-OH (1430 cm<sup>-1</sup>) and C-O (1042 cm<sup>-1</sup>). Figure. S1b exhibits the FTIR spectra of PDDA. After 100 mg and 200 mg GO were added into the PDDA solution and stirring for 12 h, the p-GO1 (Fig. S1c) and p-GO2 (Fig. S1d) were obtained. It was easy to find that the FTIR spectra of p-GO1 were similar to p-GO2. Compared to GO, the groups of GO were decreased or disappeared, such as C = O (1725 cm<sup>-1</sup>) and C-O (1042 cm<sup>-1</sup>). The results suggested the GO was successfully modified by PDDA (Wang et al. 2013b; Xu et al. 2014).

Figure. S2 shows an SEM and a TEM image of the as-prepared PB of highly uniformity cubic shape with the size of 600–900 nm. After treating the isolated PB (i.e. not on p-GO) with NaOH, the cubic crystals formed sheet-like structures (Fig. 2a). The reason is that PB has reacted with sodium hydroxide and transforms to FeOOH sheet-like structure; thus, the cubes of PB are broken. In Fig. 2d (TEM image), we can clearly see that the FeOOH sheets wrinkled together. When the PB was assembled on the PDDA-functionalized GO (the ratio of PB and GO is 1:1), the FeOOH nanosheets formed on the graphene oxide sheets (Fig. 2b) due to the strong electrostatic interaction of PB and PDDA-functionalized GO. X-ray diffraction (XRD) patterns of the precursors are shown in curve a and b in Fig. S3. The patterns of the precursors are corresponding to FeOOH (JCPDS NO. 02-0273). When the ratio of PB and GO is 1:2

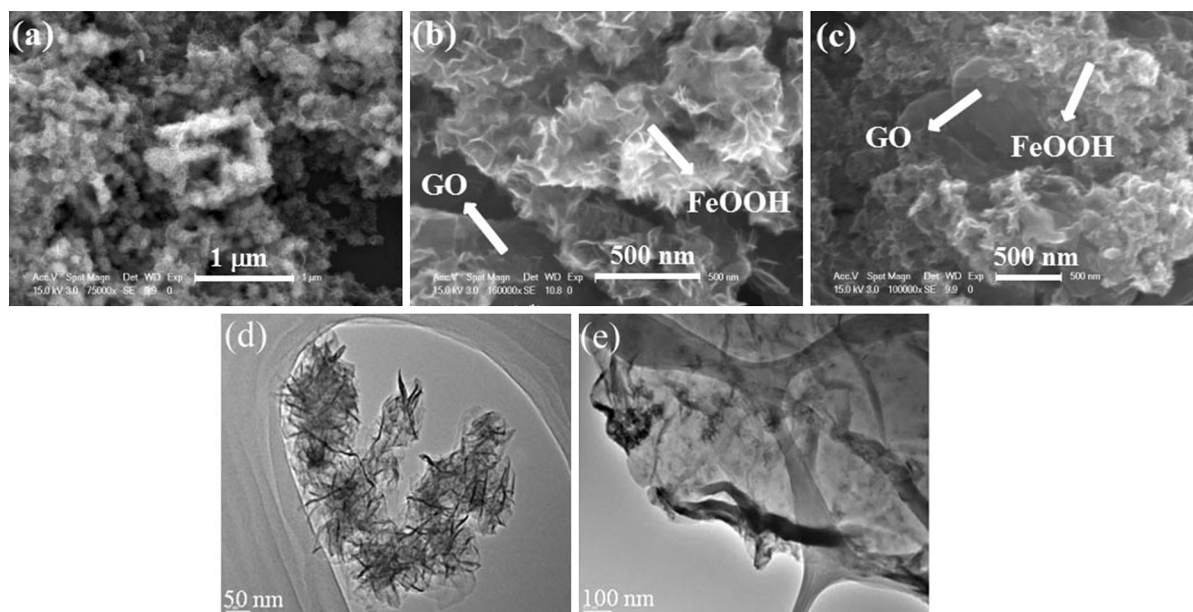


**Fig. 2** SEM images of the products after hydroxide treated with **a** PB, **b** PB/p-GO1, **c** PB/p-GO2. TEM images of **d** FeOOH sheet-like structure and **e** FeOOH/p-GO1 (with the ratio of PB and GO is 1:1)

(Fig. 2c), the morphology looks same as that in Fig. 2b. From the TEM image of FeOOH/p-GO1 (Fig. 2e), the sheet-like structures is seen laid on the graphene oxide sheets, which confirms the interaction of PB and PDDA-functionalized GO.

Raman was employed to characterize the GO before and after annealing (Fig. S4). It was easy to find that all the Raman curves had two peaks in  $1349\text{ cm}^{-1}$  (D band) and  $1593\text{ cm}^{-1}$  (G band). The  $I_d/I_g$  of GO was 0.86 (curve a in Fig. S4), while  $I_d/I_g$  of FG1 (curve b in Fig. S4) and FG2 (curve c in Fig. S4) was 1.24 and 1.17, respectively. The result suggested that the GO was reduced to rGO after thermal annealing. From Fig. 3a (sample F), we can see that after annealing FeOOH at  $500\text{ }^\circ\text{C}$ , the sheet-like structure in Fig. 2a becomes porous nanoparticles with the size about of 100–200 nm. In Fig. 3b (sample FG1), it is seen that the formed nanoparticles are decorated on the rGO, which is due to the interaction between PB and PDDA-functionalized GO. From Fig. 3c (sample FG2), we can find that the density of nanoparticles is smaller than that in Fig. 3b. This is due to the different ratio of PB and graphene oxide, larger amount of graphene oxide in FG2 will supply more position for PB and thus decrease the density of

nanoparticles. The HRTEM images of FG1 and FG2 are shown in Fig. 3d and e. The interplanar distance of FG1 and FG2 was, respectively, calculated to be 0.207 and 0.251 nm, which was accorded with the (110) and (202) lattice plane of  $\alpha\text{-Fe}_2\text{O}_3$  (JCPDS No. 79-0007).

XRD of the products after thermal treatment of FeOOH sheet-like structure and FeOOH/p-GO1 is shown in Fig. 4. For the sample without using GO, all diffraction peaks can be indexed to  $\alpha\text{-Fe}_2\text{O}_3$  (JCPDS No. 79-0007, marked as \*) with rhombohedral structure (curve a). When FeOOH nanosheets were assembled on the PDDA-functionalized GO (curve b and c), the FeOOH transformed to  $\alpha\text{-Fe}_2\text{O}_3$  (marked as \*) and  $\beta\text{-Fe}_2\text{O}_3$  (JCPDS NO. 39-0238, marked as #).

As we can see from Fig. 5a, the electrode with sample F has a high first discharge and charge capacity of 1222 and 998  $\text{mAh g}^{-1}$  (first Coulombic efficiency is 81 %), but the capacity degrades quickly during the long cycles and retains a discharge and charge capacity of 421 and 420  $\text{mAh g}^{-1}$  after 300 cycles. The first discharge and charge capacity for FG1 are 904 and 507  $\text{mAh g}^{-1}$  with a first Coulombic efficiency of 56 %. After 300 cycles, the discharge and charge capacity increased to 794 and 788  $\text{mAh g}^{-1}$  and the columbic efficiency achieved 99 %. It is noted that the capacity

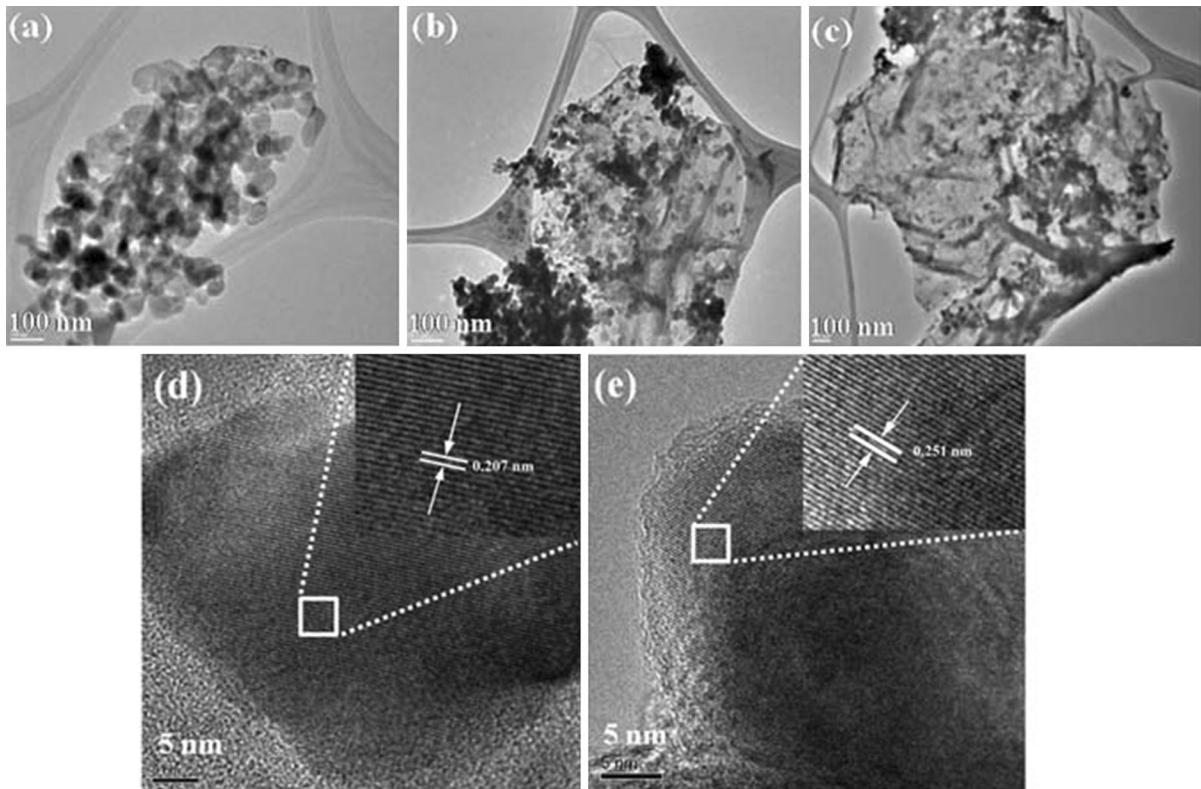


**Fig. 3** TEM images of **a** F, **b** FG1, **c** FG2. HRTEM images of **d** FG1, **e** FG2

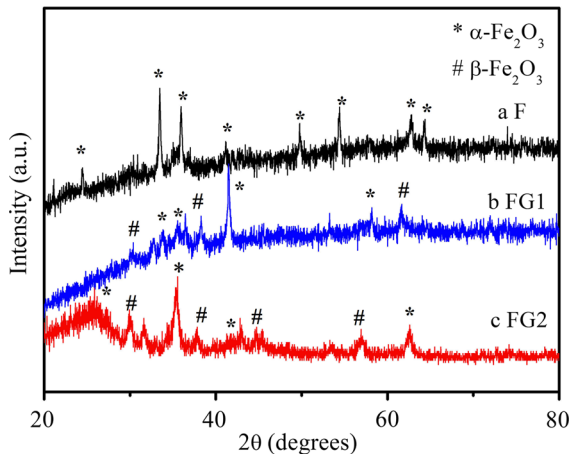


**Fig. 4** XRD of products after thermal treatment of *a* FeOOH sheet-like structure, *b* FeOOH/p-GO1 and *c* FeOOH/p-GO2

shows a steady increase with more cycles, which is due to the formation of pseudo-capacitive polymeric gel-like film and the long active process for the electrode (Kim et al. 2013). For the FG2 electrode, the first

discharge and charge capacity are 757 and 428 mAh g<sup>-1</sup>, and the value of them becomes 496 and 494 mAh g<sup>-1</sup> after 300 cycles, respectively. These results show that with incorporation of rGO, performance of the electrode can be enhanced, which is attributed to the good conductivity and buffer function of rGO during the cycling. The overall capacity of FG2 is smaller than that of FG1, which might be attributed to the low capacity of rGO than the iron oxides. The rate performance of FG1 and FG2 at different current densities is exhibited in Fig. 5b. We can see that even after large current density (2000 mA g<sup>-1</sup>) tested, the capacity can still spring back to about 580 mAh g<sup>-1</sup> for FG1 and 490 mAh g<sup>-1</sup> for FG2 at 0.1 A g<sup>-1</sup>. This indicates the good sustainability of extensive cycling at high rates for both samples.

TGA was used to study the carbon content (Fig. 6). The carbon mass loss of FG1 and FG2 was calculated to be 51 and 63 %, respectively. So the mass content of Fe<sub>2</sub>O<sub>3</sub> occupied 49 % in FG1 and 37 % in FG2. As the theoretical capacity of GO was 372 mAh g<sup>-1</sup> and that of

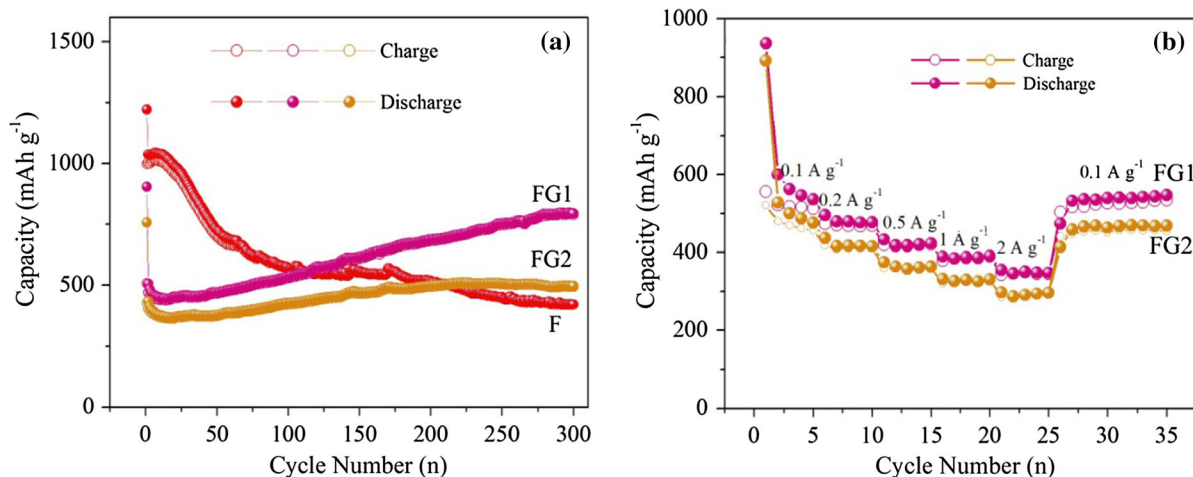


**Fig. 5** **a** Cycling performance of F, FG1 and FG2 at a current density of  $1000 \text{ mA g}^{-1}$ , **b** Rate performance of FG1 and FG2

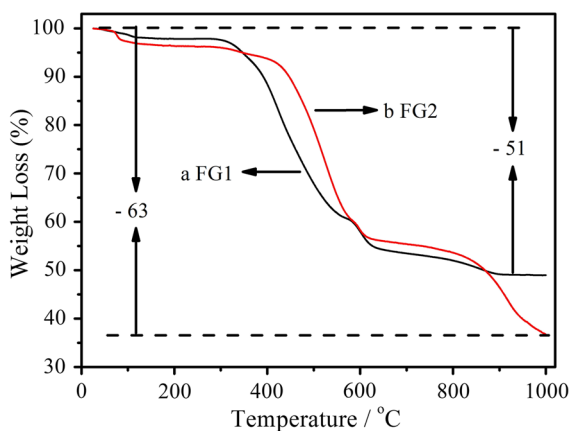


**Fig. 6** TGA curves of *a* FG1 and *b* FG2

$\text{Fe}_2\text{O}_3$  was  $1007 \text{ mAh g}^{-1}$ , so the theoretical capacity of FG1 can be calculated to be  $683.18 \text{ mAh g}^{-1}$  ( $372 \times 51\% + 1007 \times 49\% = 683.18$ ). And the theoretical capacity of FG2 was calculated to be  $606.95 \text{ mAh g}^{-1}$  by same way. So  $\text{Fe}_2\text{O}_3$  is the main contributes for the majority of the capacity.

Figure 7 shows cyclic voltammograms (CV) of F, FG1 and FG2 for the initial five cycles with a scan rate of  $0.5 \text{ mVs}^{-1}$ . The peak at  $0.65 \text{ V}$  (vs.  $\text{Li}^+/\text{Li}$ ) in the first cycle of sample F in Fig. 7a in the discharge process corresponded to reduction reaction of  $\text{Fe}^{3+}$  to  $\text{Fe}^0$  and formation of  $\text{Li}_2\text{O}$ . The peak at  $1.85 \text{ V}$  in the charging process was attributed to the oxidation reaction of  $\text{Fe}^0$ . In the subsequent cycle, the reduction

and oxidation peaks shifted slightly to  $0.8$  and  $1.65 \text{ V}$ , respectively, with decreasing peak intensity (Qiao et al. 2012). This was mainly accounted for the irreversible structural reorganization and phase formation. For CVs of samples FG1 (Fig. 7b) and FG2 (Fig. 7c), we can find same peaks appeared as Fig. 7a and some additional oxidation peaks at  $1.7$  and  $2.3 \text{ V}$ , reduction peaks at  $1.4$  and  $2.1 \text{ V}$ , which might be originated from rGO (Yang et al. 2013; Jin et al. 2016).

Figure.S5 is the first discharge–charge curves of F, FG1 and FG2. The first discharge capacity of F, FG1 and FG2 was  $1222$ ,  $904$  and  $757 \text{ mAh g}^{-1}$ , respectively. Compared to F, the FG1 and FG2 exhibited a low capacity due to the existence of rGO, which has a low theoretical capacity ( $372 \text{ mAh g}^{-1}$ ) than that of  $\text{Fe}_2\text{O}_3$  ( $1007 \text{ mAh g}^{-1}$ ). And the first discharge capacity of F is higher than the theoretical capacity, which can be attributed to the fact that the solid electrolyte interface film stored some Li ion. To study the effects of rGO in the sample of FG1 and FG2, electrochemical impedance spectroscopy (EIS) measurements of F, FG1 and FG2 were studied as shown in Fig. 7d. The electrode with F (curve a) had a largest impedance. When rGO was introduced (curve b, FG1), the impedance of the electrode becomes smaller which was due to the good electrical conductivity of rGO. With more amount of rGO (curve c, FG2), the electrode showed a smallest impedance. Although FG2 had the best electrical conductivity, it still had lower capacity than that of FG1. This was attributed to

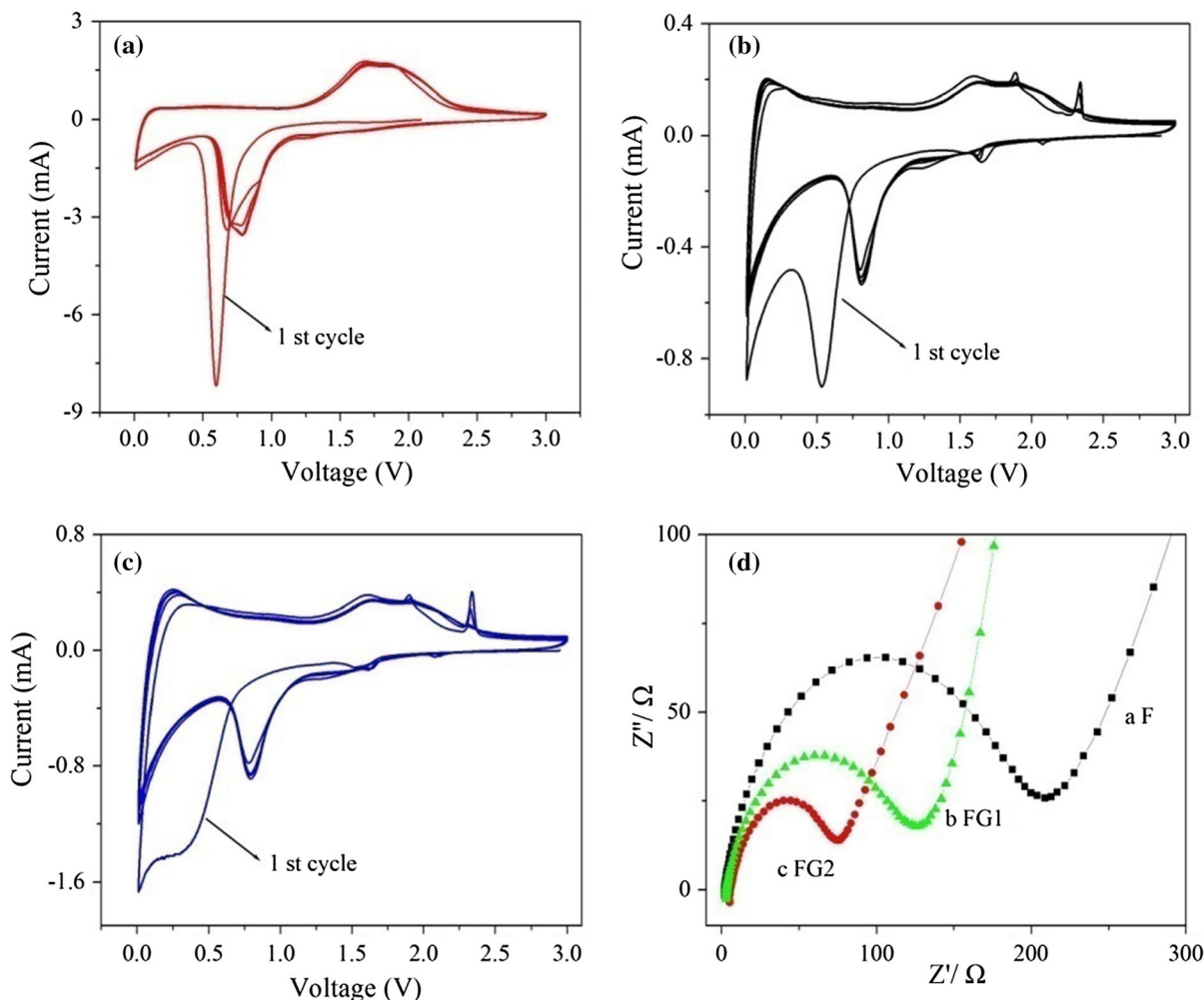


**Fig. 7** CV curves of **a** F, **b** FG1, **c** FG2, **d** Nyquist plots of cells F, FG1 and FG2 between 0.1 Hz and 1000 kHz

the lower theoretical capacity of rGO comparing to iron oxides.

## Conclusions

A self-assembly method for preparing precursors of  $\text{Fe}_2\text{O}_3/\text{rGO}$  composite for lithium-ion batteries anode was developed in this work. The  $\text{Fe}_2\text{O}_3/\text{rGO}$  composite presents a good electrochemical property which is due to the high electrical conductivity as well as the buffering role of rGO during discharge/charge processes. This study demonstrates a simple way for fabricating composites of MOFs and 2D materials for various applications.

**Acknowledgments** This project has been financially supported by National Natural Science Foundation of China (No. 51602263), Fundamental Research Funds for the Central Universities, China (XDJK2015C099, SWU114079); China Postdoctoral Science Foundation (2015M572427, 2016T90827) and Chongqing Postdoctoral Research Project (xm2015019).

## References

- Bao WZ, Zhang ZA, Qu YH, Zhou CK, Wang XW, Li J (2014) Confine sulfur in mesoporous metal–organic framework @ reduced graphene oxide for lithium sulfur battery. *J Alloys Compd* 582:334–340
- Boal AK, Ilhan F, DeRouchey JE, Albrecht TT, Russell TP, Rotello VM (2000) Self-assembly of nanoparticles into structured spherical and network aggregates. *Nature* 404:746–748

- Cao XH, Zheng B, Rui XH, Shi WH, Yan QY, Zhang H (2014) Metal oxide-coated three-dimensional graphene prepared by the use of metal-organic frameworks as precursors. *Angew Chem* 126:1428–1433
- Caruso F, Lichtenfeld H, Giersig M, Möhwald H (1998) Electrostatic self-assembly of silica nanoparticle-polyelectrolyte multilayers on polystyrene latex particles. *J Am Chem Soc* 120:8523–8524
- DeLongchamp DM, Hammond PT (2004) Multiple-color electrochromism from layer-by-layer-assembled polyaniline/prussian blue nanocomposite thin films. *Chem Mater* 16:4799–4805
- Furukawa H, Ko N, Go YB, Aratani N, Choi SB, Choi E, Yazaydin AO, Snurr RQ, O’Keeffe M, Kim J, Yaghi OM (2010) Ultrahigh porosity in metal-organic frameworks. *Science* 329:424–428
- Huang ZH, Liu GQ, Kang FY (2012) Glucose-Promoted Zn-based metal-organic framework/graphene oxide composites for hydrogen sulfide removal. *ACS Appl Mater Interfaces* 4:4942–4947
- Hummers WS Jr, Offeman RE (1958) Preparation of graphitic oxide. *J Am Chem Soc* 80:1339
- Jahan M, Liu ZL, Loh KP (2013) A graphene oxide and copper-centered metal organic framework composite as a trifunctional catalyst for HER, OER, and ORR. *Adv Funct Mater* 23:5363–5372
- Jin Y, Zhao CC, Sun ZX, Lin YC, Chen L, Wang DY, Shen C (2016) Facile synthesis of Fe-MOF/RGO and its application as a high performance anode in lithium-ion batteries. *RSC Adv* 6:30763–30768
- Kim GP, Park S, Nam I, Park J, Yi J (2013) Preferential growth of  $\text{Co}_3\text{O}_4$  anode material with improved cyclic stability for lithium-ion batteries. *J Mater Chem A* 1:3872–3876
- Kumar R, Jayaramulu K, Maji TK, Rao CNR (2013) Hybrid nanocomposites of ZIF-8 with graphene oxide exhibiting tunable morphology, significant  $\text{CO}_2$  uptake and other novel properties. *Chem Commun* 49:4947–4949
- Li JR, Kuppler R J, Zhou HC (2009) Selective gas adsorption and separation in metal-organic frameworks. *Chem Soc Rev* 38:1477–1504
- Liu Y, Qiao Y, Zhang WX, Li Z, Ji X, Miao L, Yuan LX, Hu XL, Huang YH (2015) Sodium storage in Na-rich  $\text{Na}_x\text{FeFe}(\text{CN})_6$  nanocubes. *Nano Energy* 12:386–393
- Petit C, Bandosz TJ (2011) Synthesis, characterization, and ammonia adsorption properties of mesoporous metal-organic framework (MIL(Fe))-graphite oxide composites: exploring the limits of materials fabrication. *Adv Funct Mater* 21:2108–2117
- Qiao Y, Hu XL, Huang YH (2012) Microwave-induced solid-state synthesis of  $\text{TiO}_2(\text{B})$  nanobelts with enhanced lithium-storage properties. *J Nanopart Res* 14:684–690
- Tanaka K, Muraoka T, Hirayama D, Ohnishi A (2012) Highly efficient chromatographic resolution of sulfoxides using a new homochiral MOF-silica composite. *Chem Commun* 48:8577–8579
- Wang P, Zhao J, Li XB, Yang Y, Yang QH, Li C (2013a) Assembly of ZIF nanostructures around free Pt nanoparticles: efficient size-selective catalysts for hydrogenation of alkenes under mild conditions. *Chem Commun* 49:3330–3332
- Wang Y, Zhang H, Yao D, Pu J, Zhang Y, Gao X, Sun Y (2013b) Direct electrochemistry of hemoglobin on graphene/ $\text{Fe}_3\text{O}_4$  nanocomposite-modified glass carbon electrode and its sensitive detection for hydrogen peroxide. *J Solid State Electrochem* 17:881–887
- Wang MH, Yang H, Zhou XL, Shi W, Zhou Z, Cheng P (2016) Rational design of  $\text{SnO}_2$ @C nanocomposites for lithium ion batteries by utilizing adsorption properties of MOFs. *Chem Commun* 52:717–720
- Xia FF, Hu XL, Sun YM, Luo W, Huang YH (2012) Layer-by-layer assembled  $\text{MoO}_2$ -graphene thin film as a high-capacity and binder-free anode for lithium-ion batteries. *Nanoscale* 4:4707–4711
- Xu F, Deng M, Liu Y, Ling X, Deng X, Wang L (2014) Facile preparation of poly (diallyldimethylammonium chloride) modified reduced graphene oxide for sensitive detection of nitrite. *Electrochem Commun* 47:33–36
- Yang SJ, Choi JY, Chae HK, Cho JH, Nahm KS, Park CR (2009) Preparation and enhanced hydrostability and hydrogen storage capacity of CNT@MOF-5 hybrid composite. *Chem Mater* 21:1893–1897
- Yang X, Chan CY, Xue HT, Xu J, Tang YB, Wang Q, Wong TL, Lee CS (2013) One-pot synthesis of graphene/ $\text{In}_2\text{S}_3$  nanoparticle composites for stable rechargeable lithium ion battery. *CrystEngComm* 15:6578–6584
- Zhang L, Wu HB, Lou XW (2013a) Metal-organic-frameworks-derived general formation of hollow structures with high complexity. *J Am Chem Soc* 135:10664–10672
- Zhang L, Wu HB, Xu R, Lou XWD (2013b) Porous  $\text{Fe}_2\text{O}_3$  nanocubes derived from MOFs for highly reversible lithium storage. *CrystEngComm* 15:9332–9335
- Zhao YC, Li X, Liu JD, Wang CG, Zhao YY, Yue GH (2016) MOF-Derived  $\text{ZnO}/\text{Ni}_3\text{ZnC}_{0.7}/\text{C}$  hybrids yolk-shell microspheres with excellent electrochemical performances for lithium ion batteries. *ACS Appl Mater Interfaces* 8:6472–6480
- Zhou X, Huang WY, Shi J, Zhao ZX, Xia QB, Li YW, Wang HH, Li Z (2014) A novel MOF/graphene oxide composite  $\text{GrO@MIL-101}$  with high adsorption capacity for acetone. *J Mater Chem A* 2:4722–4730
- Zhuang W, Yuan D, Liu D, Zhong C, Li JR, Zhou HC (2012) Robust metal-organic framework with an octatopic ligand for gas adsorption and separation: combined characterization by experiments and molecular simulation. *Chem Mater* 24:18–25